第43卷 第6期 岩 石 矿 物 学 杂 志 Vol. 43, No. 6: 1513~1530
2024年11月 ACTA PETROLOGICA ET MINERALOGICA Nov., 2024

Doi: 10.20086/j.cnki.yskw.2024.0609

冈底斯弧南缘侏罗纪岩浆弧地壳组成及俯冲和碰撞相关斑岩矿床成因联系

——来自Nd同位素、ΔFMQ和Eu/Eu*填图的认识

全海辉[1],柴 鹏[1],朱雄飞[2],袁玲玲[1],苏崇斌[1],李龙星[3],罗关银[3],张万元[3],徐家益[3]

(1. 中国地质科学院 地质研究所 自然资源部深地科学与探测技术实验室, 北京 100094; 2. 墨江矿业有限责任公司, 云南 墨江 654800; 3. 昌益矿业有限责任公司, 云南 墨江 654800)

摘 要: 侏罗纪岩浆弧位于冈底斯弧南缘,其中发育有侏罗纪与俯冲相关的Cu-Au和中新世与碰撞相关的Cu-Mo斑岩矿床。然而,目前对俯冲和碰撞相关的斑岩Cu矿床之间的成因联系知之甚少。本文以已发表的侏罗纪弧岩浆岩全岩主微量元素、Sm-Nd同位素和锆石微量元素数据为基础,在侏罗纪岩浆弧范围内进行了全岩Nd同位素、锆石ΔFMQ和Eu/Eu*值填图。填图结果显示,侏罗纪与俯冲相关的斑岩Cu-Au矿床主要发育区域,在侏罗纪时期具有高$\varepsilon Nd(t)$和年轻Nd模式年龄,表现出新生地壳特征,而中新世与碰撞相关的斑岩Cu-Mo矿床发育位置,在侏罗纪时期为新老地壳接触界面附近;侏罗纪斑岩Cu-Au矿床基本发育于在侏罗纪时期具有高ΔFMQ和Eu/Eu*值的岩浆区域,中新世斑岩Cu-Mo矿床发育区域的岩浆,在侏罗纪时期表现出高ΔFMQ、低Eu/Eu*值或低ΔFMQ、Eu/Eu*值的特征。这表明在侏罗纪时期,侏罗纪斑岩Cu-Au矿床所在区域的岩浆,相较于中新世斑岩Cu-Mo矿床发育区域的岩浆,具有更高的氧逸度和含水量。富水和氧化的岩浆通过抑制深部岩浆的早期硫化物饱和,为侏罗纪斑岩Cu-Au矿床的发育提供了充足的S和成矿金属。相对而言,中新世斑岩Cu-Mo矿床发育区域岩浆可能由于古老地壳组分混入而未达到抑制深部岩浆早期硫化物饱和条件,触发了早期硫化物饱,导致大量含Cu下地壳堆积形成,抑制了其在侏罗纪成矿。印度-欧亚大陆碰撞导致热软流圈熔体底侵,触发了含Cu下地壳堆晶重熔,为中新世斑岩Cu-Mo矿床的形成提供了有利的金属来源。

关键词: 斑岩铜矿; Nd同位素填图; 锆石ΔFMQ填图; 锆石Eu/Eu*填图; 侏罗纪岩浆弧

中图分类号: P618.41; P588.1 **文献标识码**: A **文章编号**: 1000-6524(2024)06-1513-18

The crustal composition of Jurassic magmatic arc in the southern margin of the Gangdise arc and the genetic relationship between subduction and collision related porphyry deposits: Insights from Nd isotope, ΔFMQ, and Eu/Eu* mapping

QUAN Hai-hui[1], CHAI Peng[1], ZHU Xiong-fei[2], YUAN Ling-ling[1], SU Chong-bin[1], LI Long-xing[3], LUO Guan-yin[3], ZHANG Wan-yuan[3] and XU Jia-yi[3]

(1. SinoProbe Laboratory of the Ministry of Natural Resources, Institute of Geology, Chinese Academy of Geological Sciences, Beijing 100094, China; 2. Mojiang Mining Co., Ltd., Mojiang 654800, China; 3. Changyi Mining Co., Ltd., Mojiang 654800, China)

收稿日期: 2024-07-12; **接受日期**: 2024-09-29; **编辑**: 郝艳丽

基金项目: 地质调查项目(DD20243512, DD20230340); 中国地质科学院基本科研业务费专项(JKYZD202312); 国家重点研发计划项目(2019YFA0708602, 2022YFF0800903)

作者简介: 全海辉(2000-), 男, 硕士研究生, 从事铜金矿勘查研究工作, E-mail: jennyq0429@163.com; 通讯作者: 柴 鹏(1988-), 男, 副研究员, 从事热液铜金矿床成矿理论研究, E-mail: cx001chaipeng@163.com。

Abstract: The Jurassic magmatic arc is located on the southern margin of the Gondwanan arc, in which Jurassic subduction-related Cu-Au and Miocene collision-related Cu-Mo porphyry deposits are developed. However, little is known about the diagenetic links between subduction- and collision-related porphyry Cu deposits. In this paper, Nd isotope, ΔFMQ and Eu/Eu^* value mapping has been carried out within the Jurassic magmatic arc, based on published whole-rock major and trace elements, Sm-Nd isotope and zircon trace elements data. The mapping results show that the main development area of Jurassic subduction-related porphyry Cu-Au deposits has high $\varepsilon Nd(t)$ and young Nd mode ages during the Jurassic period, which exhibit juvenile crustal features, while the development location of Miocene collision-related porphyry Cu-Mo deposits is near the interface of the crustal contact between the old and juvenile crust during the Jurassic period. Jurassic porphyry Cu-Au deposits were basically developed in areas with high ΔFMQ and Eu/Eu^* value magmas during the Jurassic period, and Miocene porphyry Cu-Mo deposits were developed in areas that exhibit either areas of high ΔFMQ and low Eu/Eu^* value or areas of low ΔFMQ and Eu/Eu^* values during the Jurassic period. This indicates that during the Jurassic period, the magma in the area where the Jurassic porphyry Cu-Au deposits are located had higher oxygen fugacity and water content compared to the magma in the area where the Miocene porphyry Cu-Mo deposits were developed. Water-rich and oxidised magmas provided sufficient S and metallogenic metals for the development of Jurassic porphyry Cu-Au deposits by inhibiting early sulphide saturation of deeper magmas. Comparatively, the magma of the Miocene porphyry Cu-Mo development region may have failed to reach conditions that inhibited early sulphide saturation in the deeper magma due to the mixing of ancient crustal components, which triggered early sulphide saturation, leading to the formation of large amounts of Cu-bearing lower crustal accretion and inhibiting its mineralisation in the Jurassic. The Indian-Eurasian collision resulted in the bottom intrusion of thermochondritic melts, which triggered the remelting of Cu-bearing lower crustal heap crystals, providing a favourable source of metals for the formation of the Miocene porphyry Cu-Mo deposits.

Key words: porphyry Cu deposits; Nd isotope mapping; zircon ΔFMQ mapping; zircon Eu/Eu^* mapping; Jurassic magmatic arc

Fund support: Geological Survey Project (DD20243512, DD20230340); Basic Research Funds Special Project of Chinese Academy of Geological Sciences (JKYZD202312); National Key Research and Development Program (2019YFA0708602, 2022YFF0800903)

斑岩 Cu 矿床一般发育于俯冲岩浆弧环境中(Richards, 2003; Sillitoe, 2010),并与弧岩浆的岩石成因直接相关,大多来源于交代地幔楔的部分熔融(Richards, 2009, 2011)。最近研究发现,后碰撞环境也有利于斑岩 Cu 矿床的产出(Hou *et al.*, 2009, 2015a; Richards, 2015)。前人研究表明,碰撞后斑岩 Cu 矿床的岩浆主要来源于先前大洋俯冲形成的富集金属的下地壳部分熔融(Richards, 2009, 2015; Hou *et al.*, 2015a)。尽管先前对冈底斯斑岩 Cu 矿带侏罗纪和中新世斑岩 Cu 矿床进行了诸多研究(Hou *et al.*, 2015c; Yang *et al.*, 2016; Chen *et al.*, 2019a; Zheng *et al.*, 2020, 2021; Xu *et al.*, 2022a; Wang *et al.*, 2024),但对于这两种不同时期和成因的斑岩 Cu 矿之间的联系仍然知之甚少。

东冈底斯带南缘侏罗纪岩浆弧中发育有中新世后碰撞斑岩 Cu 矿和侏罗纪俯冲相关斑岩 Cu 矿(郑有业等, 2007; Tafti *et al.*, 2009; Lang *et al.* 2014; Hou *et al.*, 2015a, 2015b; Zheng *et al.*, 2016),是研究俯冲和后碰撞斑岩 Cu 矿之间联系的天然场所。揭示深部岩石圈的物质组成和分布,特别是古老和年轻物质的分布,对于理解大型矿化体系的形成和矿化金属组合的空间分布至关重要(Hou and Zhang, 2015; 侯增谦等, 2020)。因为大型矿床形成可能与古老地壳的再造、新生地壳的重熔以及地壳熔体和流体的迁移有关(Hou and Cook, 2009; Hou *et al.*, 2015a; Xu *et al.*, 2021)。岩浆具有较高的氧逸度和含水量是利于斑岩矿床形成的两个至关重要的因素(Kelley and Cottrell, 2009; Yang *et al.*, 2016; Bao *et al.*, 2023; Xu *et al.*, 2023)。因此探究侏罗纪岩浆弧的地壳组成和岩浆氧逸度、含水量情况,对了

解研究区内俯冲和后碰撞斑岩 Cu 之间联系是必要的。

全岩 Sm-Nd 和锆石 Lu-Hf 同位素填图近年被用作评估地壳演化的工具，其能估算大陆地壳的年龄（DePaolo，1988；DePaolo *et al.*，1991；Kovalenko *et al.*，2004），并约束矿床的定位（Mole *et al.*，2014，2015；Hou *et al.*，2015a；Champion and Huston，2016）。全岩 Nd 同位素值是特定全岩样品的客观平均值，可以作为大区域同位素填图的无偏方法，比主观选择锆石的 Hf 同位素填图更具优势（侯增谦等，2018）。通过锆石微量数据计算得来的 ΔFMQ 值和 Eu/Eu^* 值分别被用作岩浆中的氧逸度和水含量的代用指标。ArcGIS 等值线填图在研究区域性问题上具有使数据可视化的优点，因此我们以收集的已发表的全岩主微量、Sm-Nd 同位素和锆石微量数据为基础，在研究区内进行 Nd 同位素、ΔFMQ 和 Eu/Eu^* 值填图，尝试探讨侏罗纪岩浆弧地壳组成及碰撞造山带中俯冲和碰撞后相关的斑岩 Cu 矿之间的成因联系。

1　地质背景

拉萨地体是组成青藏高原的东西向地体之一，北以班公湖-怒江缝合为界带与羌塘地体相隔，南至印度河-雅鲁藏布江缝合带与喜马拉雅地体相望（图 1a；Yin and Harrison，2000）。拉萨地体被狮泉河-纳木错混杂岩带（SNMZ）和洛巴堆-米拉山缝合带（LMF）分为北拉萨、中拉萨和南拉萨地体三部分（图 1b；Zhu *et al.*，2011）。北拉萨地体位于班公湖-怒江缝合带（BNSZ）和狮泉河-纳木错混杂岩带之间，被侏罗纪-白垩纪沉积岩和下白垩统火山-沉积岩系所覆盖，并有白垩纪花岗岩侵入（图 1b；Zhu *et al.*，2011；Hou *et al.*，2015a）。中拉萨地体北起狮泉河-纳木错混杂岩带，南至洛巴堆-米拉山缝合带，其主要由前寒武结晶基地和广泛分布的古生代至早白垩世沉积和火山盖层组成（图 1b；Zhu *et al.*，2013；

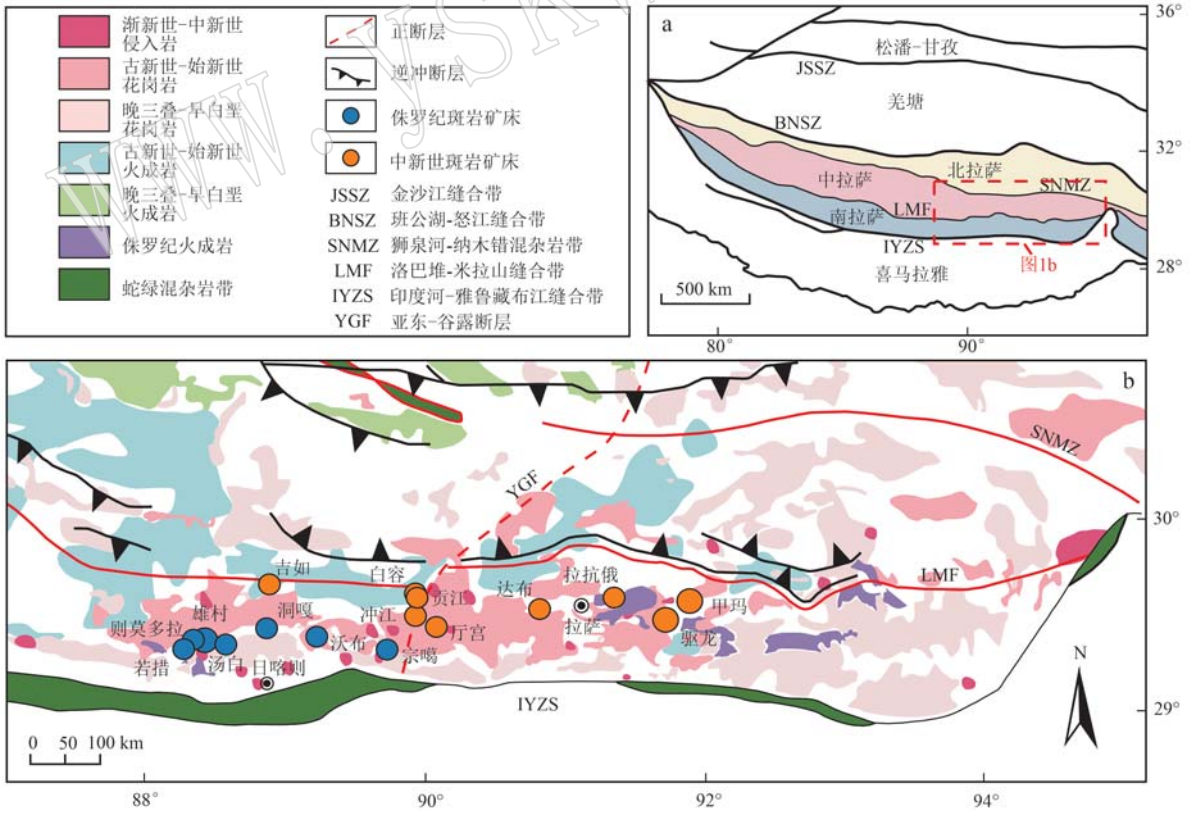

图 1　青藏高原（a，据 Zhang *et al.*，2020a 修改）和东冈底斯带区域构造图（b，据 Xu *et al.*，2020 修改）

Fig. 1　Regional tectonic map of the Qinghai-Tibet Plateau（a，modified from Zhang *et al.*，2020a）and the Eastern Gangdise Belt（b，modified from Xu *et al.*，2020）

Zhang *et al.*, 2014)。此外,其局部地区还出露少量奥陶系、志留系、泥盆系和三叠系地层作为盖层(朱弟成等, 2008; Pan *et al.*, 2012; Zhu *et al.*, 2011)。南拉萨地体处于洛巴堆-米拉山缝合带和印度河-雅鲁藏布江缝合带之间,主要由中生代和古新世-始新世火山-沉积层序(包括早侏罗世叶巴组、晚侏罗世-白垩纪桑日群、古近纪-始新世林子宗群等)及冈底斯岩基组成(图1b; Zhu *et al.*, 2011; Hou *et al.*, 2015a)。

冈底斯岩基在拉萨地体中岩浆活动最为显著,侏罗纪、白垩纪和新生代均发生了强烈的岩浆活动(Ji *et al.*, 2009; Zhu *et al.*, 2019),延伸长度约1 500 km(Wang *et al.*, 2024)。冈底斯带主要构造包括NE-SW向、NW-SE向和N-S向走滑断裂、E-W向逆冲断裂带和剪切带(图1b; Chen *et al.*, 2019a),这些构造的发育是对中新世-上新世N-S向挤压和E-W向伸展作用的响应(Coleman and Hodges, 1995; Blisniuk *et al.*, 2001)。由于新特提斯洋岩石圈早期俯冲,在冈底斯岩浆岩带东侧形成了一条长达600 km侏罗纪岩浆弧,其由大量侏罗纪侵入体及其伴生的侏罗纪火山岩构成,随后叠加了一条长达1 000 km以上的白垩纪弧(图1b; Hou *et al.*, 2015c)。侏罗纪侵入体主要由堆晶角闪辉长岩、角闪岩、角闪辉长岩、闪长岩、英云闪长岩、花岗闪长岩和二长花岗岩组成(Ji *et al.*, 2009; Zhu *et al.*, 2011; Xu *et al.*, 2019; Li *et al.*, 2022)。碰撞后的中新世埃达克质侵入体零星地分布在侏罗纪岩浆弧中,主要由孤立的岩脉、侵入的古老岩基和火山-沉积层序组成(图1b; Chung *et al.*, 2003; Hou *et al.*, 2004)。埃达克质侵入岩具有斑状结构,岩性主要为花岗闪长岩、石英二长花岗岩和花岗岩等(Wang *et al.*, 2024)。

在侏罗纪岩浆弧中识别出两期主要的斑岩成矿作用(图1b),分别是与侏罗纪弧岩套有关的Cu-Au成矿(例如雄村、东嘎和则莫多拉等; Tafti *et al.*, 2009)和与中新世后碰撞岩套相关的Cu-Mo成矿(例如甲玛、驱龙、厅宫和冲江等; Hou *et al.*, 2009)。中新世斑岩Cu矿床与侏罗纪弧存在密切的空间关系,例如驱龙、甲玛和拉抗俄等矿床均发育在侏罗纪火成岩附近(图1b)。

2 Sm-Nd同位素特征与填图

2.1 Sm-Nd同位素特征

为了最大限度地避免热液蚀变的影响,在全岩主微量和Sm-Nd同位素数据筛选时,我们尽量选择LOI<3.5%的样品,最终收集前人已发表的59个样品的Sm-Nd同位素数据,并采用同样的方法重新计算数据,具体计算方法和参数参见文献(Jacobsen and Wasserburg, 1980; Wu *et al.*, 2002)。

经校正后的$\varepsilon Nd(t)$值分布于-14.12~8.71之间,大部分大于0。在侏罗纪岩浆弧中花岗闪长岩的正$\varepsilon Nd(t)$值最大,其次是英云闪长岩,此外,大多数样品的单阶段模式年龄(t_{DM})在5.29~0.26 Ga之间,大部分岩石的$f_{Sm/Nd}$值处于-0.2~-0.5范围内(表1)。

2.2 Nd同位素等值线填图

由于数据集较小,在ArcGIS中使用反距离加权插值法对$\varepsilon Nd(t)$和t_{DM}进行等值线填图较为合理(Wang *et al.*, 2009; Mole *et al.*, 2014; Wang *et al.*, 2016)。在数据处理过程中我们尽量减少人工筛选带来的主观影响,尽可能地展现数据的原始的分布情况。对于在同一地理坐标下不同$\varepsilon Nd(t)$值的样品,为了避免ArcGIS中随机选择造成的偏差,我们采用其中位数作为作图点。因此,最终34个Nd同位素值被选为作图点。在侏罗纪时期,侏罗纪岩浆弧东部和中北部岩石的$\varepsilon Nd(t)$值多为负值,而西部和中南部岩石的$\varepsilon Nd(t)$值均为正值。最高的正$\varepsilon Nd(t)$值分布在89°E和91°E附近,其他区域正$\varepsilon Nd(t)$值大部分在0.6~6.4之间(图2)。相应的,最年轻的Nd模式年龄(0.57~0.34 Ga)出现在与正$\varepsilon Nd(t)$值相似的位置,最古老的Nd模式年龄(2.48~2.10 Ga)出现在与负$\varepsilon Nd(t)$值相似的位置(图3)。

3 锆石ΔFMQ、Eu/Eu^*特征与填图

3.1 锆石ΔFMQ、Eu/Eu^*特征

为了尽量避免LA-ICP-MS分析过程中锆石微量元素可能受到小矿物包裹体污染的影响,我们在收

表 1　东冈底斯带南缘侏罗纪岩浆岩全岩 Sm-Nd 数据

Table 1　Whole rock Sm-Nd data of Jurassic magmatic rocks in the southern margin of Eastern Gangdise Belt

岩性	年龄/Ma	$\varepsilon Nd(t)$	t_{DM}/Ma	$f_{Sm/Nd}$	数据来源
黑云母花岗岩	188.10	5.53	0.52	−0.393	Chu *et al.*, 2006
黑云母花岗岩	141.30	−9.41	1.47	−0.484	Chu *et al.*, 2006
英云闪长岩	152.00	6.91	0.38	−0.389	转引自 Hou *et al.*, 2015b
安山岩	179.00	7.10	0.40	−0.359	Chen *et al.*, 2019b
英安岩	178.90	5.27	0.52	−0.418	Chen *et al.*, 2019b
英安岩	166.70	5.78	0.48	−0.411	Chen *et al.*, 2019b
安山岩	180.20	5.84	0.55	−0.320	Chen *et al.*, 2019b
安山岩	167.80	5.78	0.57	−0.297	Chen *et al.*, 2019b
花岗闪长岩	172.40	7.06	0.39	−0.385	Chen *et al.*, 2019a
花岗闪长岩	171.60	7.26	0.39	−0.341	Chen *et al.*, 2019a
石英闪长斑岩	166.30	5.06	0.49	−0.468	Chen *et al.*, 2019a
花岗闪长岩	182.80	8.71	0.26	−0.369	Chen *et al.*, 2019a
辉长岩	192.3	6.20	0.80	−0.135	Wang *et al.*, 2017a
英云闪长岩	178.1	6.80	0.44	−0.333	Wang *et al.*, 2017a
火成岩	183	5.53	0.47	−0.472	Lang *et al.*, 2019
火成岩	183	6.27	0.50	−0.336	Lang *et al.*, 2019
角闪石英闪长玢岩	181.70	6.30	0.54	−0.278	王旭辉, 2019
石英闪长玢岩	170.00	5.70	0.50	−0.388	王旭辉, 2019
白云母二长花岗岩	191.00	−12.79	3.29	−0.198	刘琦胜等, 2006
白云母二长花岗岩	193.00	−13.77	3.88	−0.163	刘琦胜等, 2006
白云母二长花岗岩	193.00	−11.97	4.16	−0.127	刘琦胜等, 2006
白云母二长花岗岩	190.00	−11.63	2.75	−0.241	刘琦胜等, 2006
闪长岩	176.50	6.49	0.48	−0.320	李成志等, 2019
花岗闪长岩	160.00	5.38	0.46	−0.479	王莉, 2017
辉绿岩脉	165.3	4.68	0.50	−0.333	Lang *et al.*, 2018
辉绿岩脉	165.3	5.05	0.64	−0.221	Lang *et al.*, 2018
辉绿岩脉	165.3	5.56	0.43	−0.327	Lang *et al.*, 2018
辉绿岩脉	165.3	5.01	0.47	−0.335	Lang *et al.*, 2018
辉绿岩脉	165.3	5.03	0.49	−0.320	Lang *et al.*, 2018
辉绿岩脉	165.3	4.80	0.61	−0.255	Lang *et al.*, 2018
石英闪长斑岩	181	5.91	0.47	−0.428	Yin *et al.*, 2017
花岗闪长斑岩	182	0.19	0.84	−0.480	Hou *et al.*, 2015c
玄武岩	190	3.01	0.90	−0.283	Zhu *et al.*, 2008
玄武岩	189	5.70	0.69	−0.222	Kang *et al.*, 2014

集数据中筛选掉了 $La>1\times10^{-6}$ 和 $Ti>30\times10^{-6}$ 的数据，因为其可能反映样品受到磷灰石和 Ti-(Fe)氧化物的污染。最终收集西藏侏罗纪火成岩已发表的锆石微量数据共 1 267 条，然后采用统一的方法重新计算 ΔFMQ 和 Eu/Eu^* 值，具体参数参见文献(Trail *et al.*, 2011; Loucks *et al.*, 2020)：

经校正后样品的 ΔFMQ 值变化于−1.79～2.76 之间，大部分大于 0，其中含矿样品 ΔFMQ 值多数>0.53(表 2)。侏罗纪岩浆弧样品的 Eu/Eu^* 值分布于 0.013～2.143 之间，大部分小于 1，表现出中-强的 Eu 负异常(表 3)。其中含矿样品的 Eu/Eu^* 值均>0.46。

3.2　锆石 ΔFMQ、Eu/Eu^* 等值线填图

由于其数据集大小与上述 Nd 同位素填图相似，故使用上述等值线方法进行填图。为了避免 ArcGIS 随机选择所造成的偏差，我们选择同一样品不同测试点的 ΔFMQ 和 Eu/Eu^* 值的中位数作为作图值，对于在同一地理坐标下不同 ΔFMQ 和 Eu/Eu^* 值的样品，同样采用其中位数作为作图点。因此，分别筛选出 52 和 69 个样品进行 ΔFMQ 和 Eu/Eu^* 填图。侏罗纪岩浆弧在侏罗纪时期出现两个高 ΔFMQ 的岩浆区域(>0.53)和两个低 ΔFMQ 值岩浆区域(<0.53)，

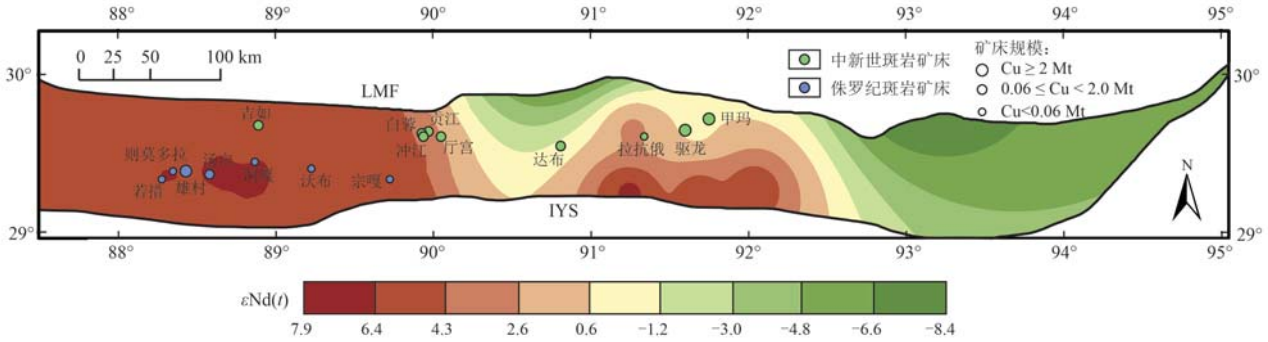

图 2 侏罗纪时期侏罗纪岩浆弧 $\varepsilon Nd(t)$ 等值线图(数据来源于表 1)

Fig. 2 Contour map of $\varepsilon Nd(t)$ for Jurassic magmatic arc of Jurassic period (data from Table 1)

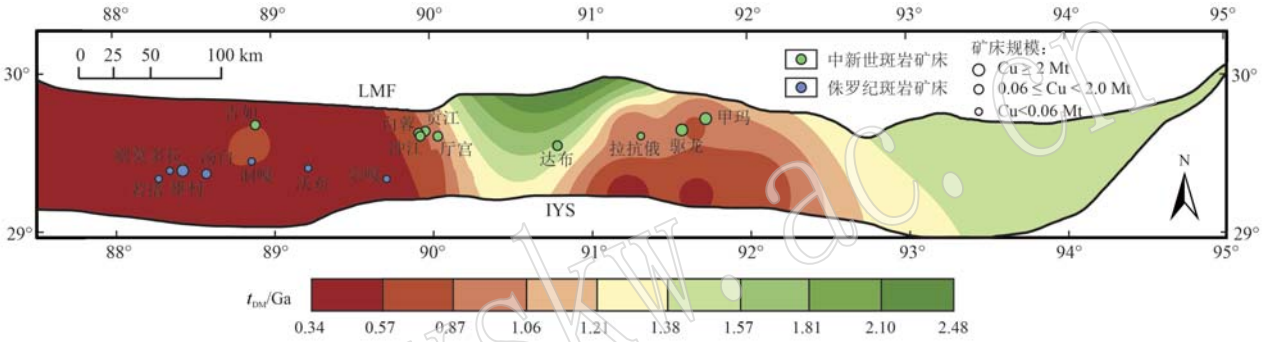

图 3 侏罗纪时期侏罗纪岩浆弧 t_{DM} 等值线图(数据来源于表 1)

Fig. 3 Contour map of t_{DM} for Jurassic magmatic arc of Jurassic period (data from Table 1)

表 2 东冈底斯带南缘侏罗纪岩浆岩锆石氧逸度数据

Table 2 Zircon oxygen fugacity data of Jurassic magmatic rocks in the southern margin of Eastern Gangdise Belt

矿床/岩体	岩性	年龄/Ma	ΔFMQ	数据来源
雄村铜金矿床	石英闪长斑岩	167.0	1.092 36	Xie *et al.*, 2018a
雄村铜金矿床	角闪石英闪长斑岩	170.8	1.204 419	Xie *et al.*, 2023
雄村铜金矿床	角闪石英闪长斑岩	165.4	1.276 526	Chen *et al.*, 2019a
雄村铜金矿床	英安岩	178.9	0.747 792	Chen *et al.*, 2019b
雄村铜金矿床	英安岩	174.3	1.733 752	Chen *et al.*, 2019b
雄村铜金矿床	英安岩	166.7	1.705 461	Chen *et al.*, 2019b
雄村铜金矿床	安山岩	178.3	1.055 09	Chen *et al.*, 2019b
雄村铜金矿床	安山岩	180.2	1.031 607	Chen *et al.*, 2019b
彭措林	花岗闪长岩	175.8	1.289 089	Xie *et al.*, 2018b
彭措林	花岗闪长岩	165.4	1.052 265	Xie *et al.*, 2023
若措	角闪石英闪长斑岩	178.5	0.959 213	Xie *et al.*, 2023
彭措林	花岗闪长岩	169.0	1.672 1	Yu *et al.*, 2022
谢通门	花岗闪长岩	172.4	0.727 591	Chen *et al.*, 2019a
谢通门	花岗闪长岩	171.6	1.865 743	Chen *et al.*, 2019a
谢通门	石英闪长斑岩	178.9	0.321 347	Chen *et al.*, 2019a
塔玛	花岗闪长岩	182.8	0.488 125	Chen *et al.*, 2019a
汤白	花岗闪长岩	178.7	1.185 177	Chen *et al.*, 2019a
汤白	石英闪长斑岩	181.8	1.243 227	Chen *et al.*, 2019a
桑日	花岗闪长岩	184.5	−0.138 21	Chen *et al.*, 2019a
崔久	花岗闪长岩	192.1	−0.110 81	Chen *et al.*, 2019a
驱龙	石英闪长斑岩	173.0	2.762 355	Chen *et al.*, 2019a

续表 2

Continued Table 2

矿床/岩体	岩性	年龄/Ma	ΔFMQ	数据来源
现巴塘	花岗闪长岩	195.3	0.039 409	Chen *et al.*, 2019a
雄村铜金矿床	石英正长斑岩	173.7	0.897 947	邹银桥等, 2015
雄村铜金矿床	闪长岩	167.3	1.448 343	Wang *et al.*, 2017b
雄村铜金矿床	花岗闪长岩	168.0	0.710 469	Wang *et al.*, 2017b
雄村铜金矿床	花岗闪长岩	172.2	1.910 79	Wang *et al.*, 2017b
雄村铜金矿床	花岗闪长岩	169.5	1.451 311	Wang *et al.*, 2017b
沃卡	花岗闪长岩	182.3	0.182 558	Wang *et al.*, 2017b
加查	花岗闪长岩	173.0	0.097 424	Wang *et al.*, 2017b
加查	花岗闪长岩	181.0	0.088 853	Wang *et al.*, 2017b
汤白	花岗闪长岩	168.8	0.846 168	Wang *et al.*, 2017b
日喀则	花岗闪长岩	170.3	0.503 648	Wang *et al.*, 2017b
驱龙	花岗斑岩	185.0	1.503 188	Wang *et al.*, 2017b
泽嘎	二长花岗岩	200.0	−1.797 47	Wang *et al.*, 2017b
南木林	花岗岩	184.0	0.914 055	Wang *et al.*, 2017b
芒热	二长花岗岩	200.0	0.673 388	Wang *et al.*, 2017b
雄村铜金矿床	石英闪长斑岩	166.3	1.312 034	Chen *et al.*, 2020
雄村铜金矿床	石英闪长斑岩	175.5	1.270 37	Chen *et al.*, 2020
叶巴组	流纹凝灰岩	173.3	1.240 125	Ma *et al.*, 2017a
叶巴组	流纹凝灰岩	169.4	1.295 778	Ma *et al.*, 2017a
叶巴组	安山质凝灰岩	174.3	0.251 748	Ma *et al.*, 2017a
桑巴	花岗闪长岩	176.2	−0.066 19	Xie *et al.*, 2018b
大竹曲	二长花岗岩	159.4	−1.058 14	Xie *et al.*, 2018b
大竹曲	安山岩	188.6	0.108 525	Xie *et al.*, 2023
曲瓦达	花岗闪长岩	194.0	−0.069 92	Xie *et al.*, 2018b
达夏	石英闪长斑岩	188.2	−0.439 68	Xie *et al.*, 2018b
卫堆	石英闪长岩	181.7	0.095 681	Xie *et al.*, 2023
卫堆	花岗岩	181.0	−0.278 07	Xie *et al.*, 2023
卫堆	花岗岩	183.5	0.677 63	Xie *et al.*, 2023
斑鸠林	闪长岩	189.9	0.739 495	Xie *et al.*, 2023
叶巴组	流纹凝灰岩	174.6	1.239 902	Ma *et al.*, 2017b
叶巴组	安山质凝灰岩	179.8	0.250 804	Ma *et al.*, 2017b

表 3　东冈底斯带南缘侏罗纪岩浆岩锆石 Eu/Eu* 数据

Table 3　Zircon Eu/Eu* data of Jurassic magmatic rocks in the southern margin of Eastern Gangdise Belt

矿床/岩体	岩性	年龄/Ma	Eu/Eu*	数据来源
雄村铜金矿床	石英闪长斑岩	171.5	0.708 826	Xie *et al.*, 2023
雄村铜金矿床	角闪石英闪长斑岩	171.7	0.666 274	Xie *et al.*, 2023
雄村铜金矿床	含粗石英眼角闪石英闪长斑岩	174.4	0.724 164	Xie *et al.*, 2018a
雄村铜金矿床	角闪石英闪长斑岩	175.9	0.658 551	Chen *et al.*, 2019a
雄村铜金矿床	英安岩	178.9	0.577 119	Chen *et al.*, 2019b
雄村铜金矿床	英安岩	174.3	0.643 583	Chen *et al.*, 2019b
雄村铜金矿床	英安岩	166.7	0.669 681	Chen *et al.*, 2019b
雄村铜金矿床	安山岩	181.6	0.543 570	Chen *et al.*, 2019b
雄村铜金矿床	安山岩	180.2	0.555 368	Chen *et al.*, 2019b
彭措林	花岗闪长岩	175.5	0.733 747	Xie *et al.*, 2018b
彭措林	花岗闪长岩	174.2	0.730 348	Xie *et al.*, 2023
若措	角闪石英闪长斑岩	175.0	0.781 418	Xie *et al.*, 2023
彭措林	花岗闪长岩	169.0	0.694 462	Yu *et al.*, 2022
谢通门	花岗闪长岩	172.4	0.822 037	Chen *et al.*, 2019a
谢通门	花岗闪长岩	171.6	0.569 748	Chen *et al.*, 2019a
谢通门	石英闪长斑岩	178.9	0.793 624	Chen *et al.*, 2019a

续表 3

Continued Table 3

矿床/岩体	岩性	年龄/Ma	Eu/Eu*	数据来源
塔玛	花岗闪长岩	182.8	0.613 826	Chen *et al.*, 2019a
汤白	花岗闪长岩	178.7	0.566 766	Chen *et al.*, 2019a
汤白	花岗闪长斑岩	181.8	0.550 939	Chen *et al.*, 2019a
桑日	石英闪长斑岩	184.5	0.506 206	Chen *et al.*, 2019a
崔久	花岗闪长岩	192.1	0.514 965	Chen *et al.*, 2019a
驱龙	花岗闪长斑岩	173.0	0.448 592	Chen *et al.*, 2019a
现巴塘	石英闪长岩	195.3	0.592 404	Chen *et al.*, 2019a
雄村铜金矿床	石英正长斑岩	173.7	0.611 855	邹银桥等,2015
雄村铜金矿床	闪长岩	167.3	0.598 292	Wang *et al.*, 2017b
雄村铜金矿床	花岗闪长岩	168.0	0.698 789	Wang *et al.*, 2017b
雄村铜金矿床	花岗闪长岩	172.2	0.629 763	Wang *et al.*, 2017b
雄村铜金矿床	花岗闪长岩	169.5	0.793 038	Wang *et al.*, 2017b
沃卡	花岗闪长岩	182.3	0.221 281	Wang *et al.*, 2017b
加查	花岗闪长岩	173.0	0.452 099	Wang *et al.*, 2017b
加查	花岗闪长岩	185.5	0.702 092	Wang *et al.*, 2017b
汤白	花岗闪长岩	168.8	0.427 249	Wang *et al.*, 2017b
日喀则	花岗闪长岩	170.3	0.501 403	Wang *et al.*, 2017b
驱龙	花岗斑岩	185.0	0.293 278	Wang *et al.*, 2017b
泽嘎	二长花岗岩	200.0	0.396 378	Wang *et al.*, 2017b
南木林	花岗岩	191.0	0.158 313	Wang *et al.*, 2017b
芒热	二长花岗岩	200.0	0.352 273	Wang *et al.*, 2017b
雄村铜金矿床	石英闪长斑岩	166.3	0.599 236	Chen *et al.*, 2020
雄村铜金矿床	石英闪长斑岩	175.5	0.707 504	Chen *et al.*, 2020
叶巴组	流纹质凝灰岩	173.3	0.306 793	Ma *et al.*, 2017b
叶巴组	流纹质凝灰岩	169.4	0.309 770	Ma *et al.*, 2017b
叶巴组	安山质凝灰岩	174.3	0.312 842	Ma *et al.*, 2017b
桑巴	花岗闪长岩	176.2	0.534 564	Xie *et al.*, 2018b
大竹曲	二长岩	159.4	0.169 560	Xie *et al.*, 2018b
大竹曲	安山岩	193.9	0.516 904	Xie *et al.*, 2023
曲瓦达	花岗闪长岩	185.1	0.530 446	Xie *et al.*, 2018b
达夏	石英闪长斑岩	202.4	0.201 458	Xie *et al.*, 2018b
达夏	凝灰岩	187.5	0.428 230	Xie *et al.*, 2023
斑鸠林	闪长岩	174.9	0.528 119	Xie *et al.*, 2023
加查崔久沟	花岗闪长岩	196.5	0.528 095	董昕等, 2013
桑日沃卡电站	花岗闪长岩	180.0	0.815 119	董昕等, 2013
达孜	英安岩	176.4	0.271 062	Wang *et al.*, 2024
叶巴组	安山岩	170.1	0.382 650	Wang *et al.*, 2024
思布	安山岩	167.0	0.260 529	Wang *et al.*, 2024
甲玛	英安岩	173.6	0.436 831	Wang *et al.*, 2024
思布	安山岩	171.3	0.420 222	Wang *et al.*, 2024
思布	安山岩	179.4	0.335 688	Wang *et al.*, 2024
叶巴组	安山岩	182.2	0.274 496	Wang *et al.*, 2024
谢通门	花岗闪长岩	174.5	0.602 198	Wang *et al.*, 2024
谢通门	花岗闪长岩	172.0	0.651 223	Wang *et al.*, 2024
谢通门	花岗闪长岩	163.0	0.465 074	Wang *et al.*, 2024
叶巴组	安山岩	186.9	0.245 224	Wang *et al.*, 2024
加查	石英闪长岩	198.1	0.490 654	Wang *et al.*, 2024
叶巴组	流纹质凝灰岩	177.4	0.306 793	Ma *et al.*, 2017b
叶巴组	流纹质凝灰岩	170.1	0.309 770	Ma *et al.*, 2017b
叶巴组	安山质凝灰岩	174	0.312 842	Ma *et al.*, 2017b
	花岗片麻岩	165	0.307 071	Guo *et al.*, 2011
	岩浆岩	189	0.404 257	Wang *et al.*, 2019
	岩浆岩	174.4	0.287 373	转引自 Hou *et al.*, 2015b

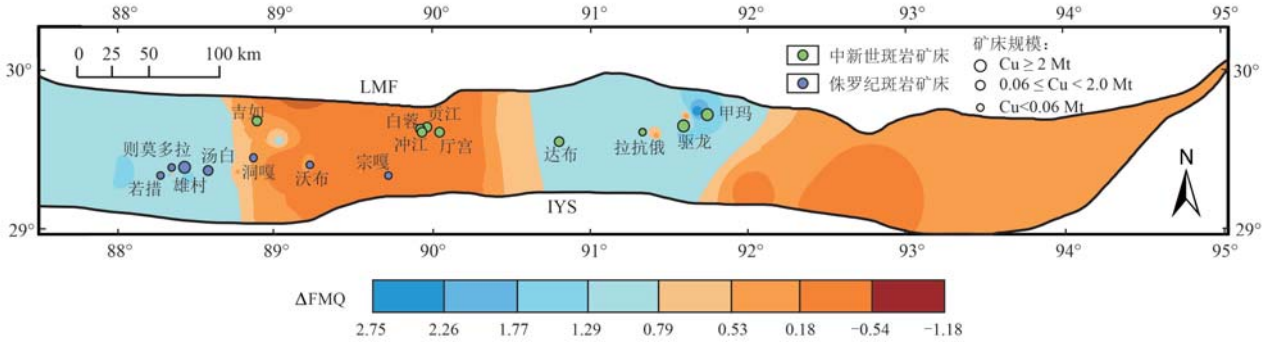

图 4　侏罗纪时期侏罗纪岩浆弧锆石 ΔFMQ 填图(数据来源于表 2)

Fig. 4　Contour map of zircon ΔFMQ for Jurassic magmatic arc of Jurassic period (data from Table 2)

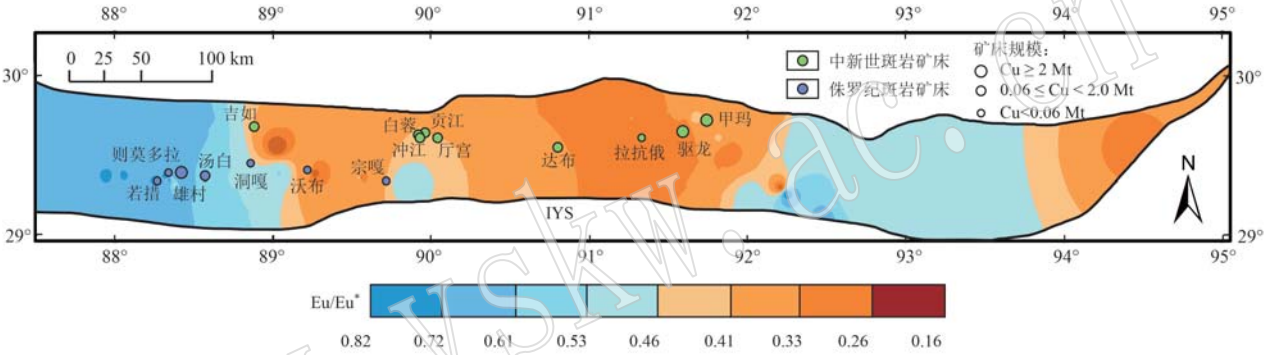

图 5　侏罗纪时期侏罗纪岩浆弧锆石 Eu/Eu* 填图(数据来源于表 3)

Fig. 5　Contour map of zircon Eu/Eu* for Jurassic magmatic arc of Jurassic period (data from Table 3)

最高的 ΔFMQ 值位于 88°E 和甲玛矿床附近,最低值分布在 89°E 右侧(图 4)。填图结果显示(图 5),88.7°E 左侧和 92.3°E～93.6°E 附近出现两个高 Eu/Eu* 值岩浆区域(>0.46),低 Eu/Eu* 值岩浆区域主要分布在岩浆弧中部和最东侧,大部分低值区 Eu/Eu* 值在 0.26～0.46 之间。

4　讨论

4.1　地壳组分的分布与形成

近年来,Nd 同位素数据被用来区别年轻地壳组分和古老地壳组分(Wang *et al.*, 2009; Mole *et al.*, 2015; 侯增谦等, 2018; Granseth *et al.*, 2021)。年轻地壳的 $\varepsilon Nd(t)$ 值位于或接近于亏损地幔演化线,被认为是直接从亏损地幔中产生或最近从亏损地幔中提取的物质重熔而成(Yuan *et al.*, 2023)。然而,古老或改造的地壳是指通过部分熔融和/或侵蚀与沉积作用重新活化的先存地壳(Belousova *et al.*, 2010; Hawkesworth *et al.*, 2010; Hou *et al.*, 2015a)。Sm-Nd 同位素体系的母体和子体元素均为稀土元素(REEs),且具有一定相似性,可以有效地指示地壳过程和岩石来源(DePaolo, 1988; Champion, 2013)。在新生地壳形成过程中,由于镧系收缩,地幔比地壳储库具有更低的 Sm/Nd 值,导致 $\varepsilon Nd(t)$ 值随时间变化(Champion, 2013)。因此,$\varepsilon Nd(t)$ 值和 Nd 模式年龄分别被作为示踪岩浆来源和地壳源岩形成时代的工具(侯增谦等, 2018)。

侏罗纪岩浆弧中 90°E 往左和 91°～92°E 附近,在侏罗纪时期具有高 $\varepsilon Nd(t)$ 值和低 Nd 模式年龄(图 2、图 3),表明这些区域在侏罗纪时期发育有新生地壳,同时也指示了该区域在存在地壳生长,其可能是新特提斯洋俯冲期间幔源弧岩浆注入导致地壳垂向生长的结果(Zhang *et al.*, 2020b; 侯增谦等, 2020)。古老地壳在侏罗纪时期主要分布在 90°～91°E 附近和 92.5°E 右侧的低 $\varepsilon Nd(t)$ 值和高 Nd 模式年龄区域(图 2、图 3)。Nd 同位素填图结果显示,

侏罗纪时期在新生地壳和古老地壳之间存在一个重要的新、老地壳边界(图2、图3)。

在俯冲带,弧岩浆会受到前期岩浆作用形成的围岩的同化混染作用,会导致弧火成岩 Nb/Th 和 Nb/La 值的降低(Zhang *et al.*, 2017)。相较于新生地壳区域,新老地壳接触边界附近具有较低的 Nb/Th 和 Nb/La 值(图6),这可能暗示了在地壳接触边界发生了新老地壳混合作用。在新老地壳接触

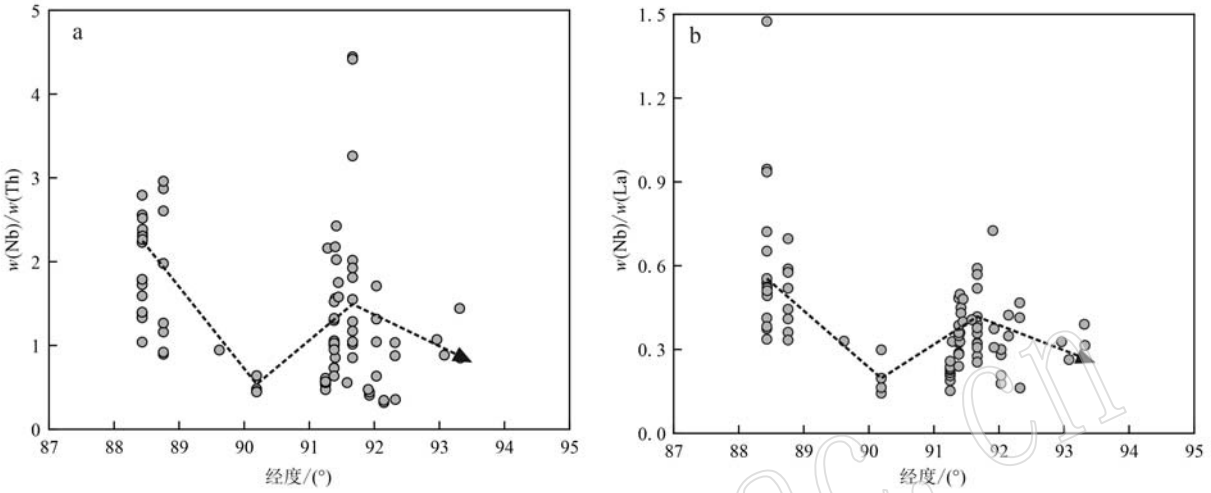

图6 侏罗纪火成岩的 Nb/Th-经度(a)和 Nb/La-经度(b)图解(数据来源于表4)

Fig. 6 Nb/Th-longitude (a) and Nb/La-longitude (b) diagrams of Jurassic igneous rocks (data from Table 4)

边界,中新世与成矿相关斑岩的 $\varepsilon Nd(t)$ 值显示出逐渐降低的趋势(Hou *et al.*, 2015b),也指示了少量古老地壳混合。

4.2 填图对侏罗纪成矿的指示

探究侏罗纪岩浆弧氧逸度和含水量情况,对于厘清侏罗纪斑岩成矿及其对中新世斑岩矿床形成的贡献具有重要意义。锆石 ΔFMQ 和 Eu/Eu^* 值通常被用来指示岩浆氧逸度的高低(Ballard *et al.*, 2002; Bao *et al.*, 2023; Xu *et al.*, 2023)。然而最近研究表明,锆石 Eu/Eu^* 值在很大程度上受锆石沉淀前或沉淀过程中结晶的其他含稀土元素相的控制(Loader *et al.*, 2017; Lu *et al.*, 2019; Rezeau *et al.*, 2019; Turlin *et al.*, 2019; Groulier *et al.*, 2020; Nathwani *et al.*, 2021),氧化还原条件对锆石 Eu/Eu^* 比值起次要作用(Nathwani *et al.*, 2021)。在熔体中具有较高水含量(>4%)的条件下,会导致角闪石的早期结晶和分馏以及抑制地壳深部斜长石的结晶(Moore and Carmichael, 1998; Müntener *et al.*, 2001; Ridolfi *et al.*, 2010),因此锆石 Eu/Eu^* 值也可作为岩浆中水含量的代用指标(Lu *et al.*, 2019; Wu *et al.*, 2021)。

锆石 ΔFMQ 和 Eu/Eu^* 填图结果显示,侏罗纪斑岩 Cu 矿床主要分布区域的岩浆在侏罗纪时期具有高 ΔFMQ 和 Eu/Eu^* 值(图3、图4),说明该区域岩浆具有较高的氧逸度和水含量。有趣的是,中新世斑岩 Cu 矿床分布区域的岩浆 ΔFMQ 值在侏罗纪时期从高到低均有分布,但均具有较低的 Eu/Eu^* 值(图3、图4),这表明中新世斑岩 Cu 矿床所在区域岩浆在侏罗纪时期既有高氧逸度也存在低氧逸度,且岩浆中水含量均较低。从上述填图结果显示,低氧逸度地区大多为侏罗纪时期古老地壳或新老地壳接触边界附近(图2、图3、图4),这可能是由于古老地壳混入导致岩浆氧逸度降低(Hou and Zhang, 2015)。91°~92°E 高氧逸度岩浆区域和侏罗纪新生地壳区域基本对应(图2、图3、图4),说明侏罗纪岩浆弧在新特提斯洋俯冲期间的地壳生长过程可能促进了岩浆氧逸度的提升,即在俯冲期间板片来源的氧化流体加入到岩浆源区提升了其氧逸度(Kelley and Cottrell, 2009; Brounce *et al.*, 2014; Zhang *et al.*, 2021)。侏罗纪斑岩矿床大多数分布于高氧逸度和含水量岩浆区域,这归结于在新特提斯洋的北向俯冲过程中,富水和富氧的板片流体的加入,导致被交代的软流圈地幔发生低程度的部分熔融(Wang *et al.*, 2017a; 郎兴海等, 2019; Yu *et al.*, 2022),形成了富水、S、Cl、氧化且含金属的镁铁质岩浆(Davidson, 1996; de Hoog *et al.*, 2001; Xu *et al.*, 2017),这种岩浆因密度较低而上升形成了斑岩型 Cu-Au 矿床(Richards, 2003)。然而,中新世斑岩矿

表 4　东冈底斯带南缘侏罗纪岩浆岩主、微量数据

Table 4　Main and trace element data of Jurassic magmatic rocks in the southern margin of Eastern Gangdise Belt

岩性	年龄/Ma	烧失量	Nb/La	Nb/Th	数据来源
黑云母花岗岩	188.10		0.329 87	0.945 996	Chu *et al.*, 2006
流纹岩	174.40	1.99	0.276 549	1.285 533	董国臣等, 2006
流纹岩	174.40	1.62	0.254 761	1.015 177	董国臣等, 2006
流纹岩	174.40	3.08	0.391 447	3.260 274	董国臣等, 2006
流纹岩	174.40	2.07	0.323 264	1.046 371	董国臣等, 2006
流纹岩	174.40	1.59	0.519 023	1.924 211	董国臣等, 2006
流纹岩	174.40	1.60	0.320 565	0.853 309	董国臣等, 2006
流纹岩	174.40	1.48	0.307 314	1.045 759	董国臣等, 2006
流纹岩	174.40	2.61	0.417 391	1.811 321	董国臣等, 2006
流纹岩	174.40	1.81	2.360 434	4.443 878	董国臣等, 2006
流纹岩	174.40	1.24	0.357 772	1.171 916	董国臣等, 2006
流纹岩	174.40	3.31	0.568 45	4.415 493	董国臣等, 2006
花岗闪长岩	168.00	0.78	0.361 585	1.160 47	Guo *et al.*, 2011
花岗闪长岩	170.00	0.57	0.333 784	1.266 667	Guo *et al.*, 2011
花岗闪长岩	172.00	1.04	0.696 629	1.978 723	Guo *et al.*, 2011
花岗闪长岩	178.00	1.07	0.409 548	0.895 604	Guo *et al.*, 2011
英云闪长岩	178.00	0.96	0.588 608	2.870 37	Guo *et al.*, 2011
英云闪长岩	180.00	1.14	0.576 24	2.959 119	Guo *et al.*, 2011
英云闪长岩	181.00	0.39	0.443 902	0.919 192	Guo *et al.*, 2011
英云闪长岩	182.00	1.80	0.519 293	2.604 839	Guo *et al.*, 2011
英安岩	171.9	2.00	0.287 298	1.055 666	Hou *et al.*, 2015b
英安岩	171.9	1.51	0.323 956	0.999 209	Hou *et al.*, 2015b
英安岩	171.9	1.80	0.337 062	1.023 08	Hou *et al.*, 2015b
英安岩	171.9	1.93	0.282 599	1.021 592	Hou *et al.*, 2015b
石英闪长斑岩	173.00		1.532 738	1.778 929	转引自 Hou *et al.*, 2015b
石英闪长斑岩	173.00		1.474 453	2.556 962	转引自 Hou *et al.*, 2015b
石英闪长斑岩	173.00		2.192 067	2.792 553	转引自 Hou *et al.*, 2015b
石英闪长斑岩	173.00		0.652 33	1.725 118	转引自 Hou *et al.*, 2015b
石英闪长斑岩	173.00		0.721 659	1.393 238	转引自 Hou *et al.*, 2015b
石英闪长斑岩	173.00		0.538 344	1.04	转引自 Hou *et al.*, 2015b
安山岩	195	2.07	0.3	1.710 28	Kang *et al.*, 2014
安山岩	195	1.75	0.207 177	1.043 373	Kang *et al.*, 2014
石英闪长斑岩	164.3	2.19	0.935 356	2.229 56	郎兴海等, 2010
石英闪长斑岩	173	0.7	0.412 796	1.342 065	郎兴海等, 2010
石英闪长斑岩	173.00	1.99	0.553 913	1.592 5	郎兴海等, 2010
石英闪长斑岩	175	2.36	0.336 842	1.379 768	曲晓明等, 2006
石英闪长斑岩	175	1	0.374 336	1.330 189	曲晓明等, 2006
石英闪长斑岩	179	1.56	0.382 063	1.396 721	曲晓明等, 2006
花岗闪长岩	145	0.88	0.349 709	0.499 316	Hou *et al.*, 2015a
花岗闪长岩	145	1.10	0.284 747	0.540 734	Hou *et al.*, 2015a
花岗闪长岩	159	1.33	0.751 542	1.470 506	Hou *et al.*, 2015a
花岗闪长岩	159	2.04	0.788 764	1.749 763	Hou *et al.*, 2015a
花岗闪长岩	162	2.01	0.427 709	0.929 31	Hou *et al.*, 2015a
花岗闪长岩	162	1.79	0.364 746	0.803 042	Hou *et al.*, 2015a
花岗岩	163	1.80	0.422 841	0.318 096	Hou *et al.*, 2015a
花岗岩	163	1.26	0.347 946	0.345 241	Hou *et al.*, 2015a
安山岩	172	2.00	0.287 298	1.055 666	Hou *et al.*, 2015a
安山岩	172	1.51	0.323 956	0.999 209	Hou *et al.*, 2015a
安山岩	172	1.80	0.337 062	1.023 08	Hou *et al.*, 2015a

续表 4

Continued Table 4

岩性	年龄/Ma	烧失量	Nb/La	Nb/Th	数据来源
安山岩	172	1.93	0.282 599	1.021 592	Hou *et al.*, 2015a
凝灰岩	173	1.33	0.502 558	2.334 475	Hou *et al.*, 2015a
凝灰岩	173	1.25	0.523 754	2.517 201	Hou *et al.*, 2015a
凝灰岩	173	1.36	0.520 101	2.385 767	Hou *et al.*, 2015a
凝灰岩	173	1.19	0.492 567	2.304 631	Hou *et al.*, 2015a
凝灰岩	173	1.05	0.510 51	2.264 618	Hou *et al.*, 2015a
花岗岩	194	0.56	0.374 247	0.406 281	Hou *et al.*, 2015a
花岗岩	194	0.55	0.307 497	0.442 4	Hou *et al.*, 2015a
花岗闪长岩	198	1.68	0.466 975	1.035 035	Hou *et al.*, 2015a
花岗闪长岩	198	2.25	0.414 123	0.877 558	Hou *et al.*, 2015a
英云闪长岩	152.00	2.00	0.212 969	0.570 698	转引自 Hou *et al.*, 2015b
英云闪长岩	152.00	1.50	0.236 111	0.603 738	转引自 Hou *et al.*, 2015b
英云闪长岩	152.00	1.61	0.188 655	0.541 133	转引自 Hou *et al.*, 2015b
英云闪长岩	152.00	2.77	0.214 051	0.578 014	转引自 Hou *et al.*, 2015b
英云闪长岩	152.00	3.05	0.208 955	0.555 372	转引自 Hou *et al.*, 2015b
英云闪长岩	152.00	2.58	0.211 021	0.529 042	转引自 Hou *et al.*, 2015b
英云闪长岩	152.00	2.03	0.152 425	0.472 103	转引自 Hou *et al.*, 2015b
英云闪长岩	152.00	1.94	0.205 823	0.556 777	转引自 Hou *et al.*, 2015b
英云闪长岩	152.00	1.70	0.225 997	0.583 969	转引自 Hou *et al.*, 2015b
英云闪长岩	152.00	2.40	0.230 715	0.586 453	转引自 Hou *et al.*, 2015b
英云闪长岩	152.00	2.50	0.237 516	0.608 197	转引自 Hou *et al.*, 2015b
花岗斑岩	182.30	0.77	0.239 865	0.733 471	杨志明等, 2011
花岗斑岩	182.30	0.52	0.483 916	1.298 311	杨志明等, 2011
花岗斑岩	182.30	0.74	0.324 265	0.730 132	杨志明等, 2011
花岗斑岩	182.30	1.13	0.385 987	0.635 22	杨志明等, 2011
花岗岩	178.00	0.26	0.143 64	0.479 853	张宏飞等, 2007
花岗岩	178.00	0.29	0.164 07	0.449 749	张宏飞等, 2007
花岗岩	178.00	0.39	0.197 066	0.445 245	张宏飞等, 2007
花岗岩	178.00	0.37	0.299 056	0.639 013	张宏飞等, 2007
安山岩	174.2	2.48	0.328 431	2.161 29	Zhu *et al.*, 2008
英安岩	174.2	1.47	0.430 189	2.425 532	Zhu *et al.*, 2008
英安岩	174.2	1.97	0.328 025	1.560 606	Zhu *et al.*, 2008
英安岩	174.2	2.75	0.360 153	0.854 545	Zhu *et al.*, 2008
英安岩	174.2	1.94	0.348 837	0.949 367	Zhu *et al.*, 2008
英安岩	174.2	4.23	0.359 606	1.520 833	Zhu *et al.*, 2008
英安岩	174.2	1.68	0.386 266	1.323 529	Zhu *et al.*, 2008
英安岩	174.2	2.97	0.480 687	1.577 465	Zhu *et al.*, 2008
流纹岩	146.10	1.30	0.365 199	0.655 829	Zhu *et al.*, 2011
正长花岗岩	152.90	0.69	0.698 422	0.524 338	Zhu *et al.*, 2011
英云闪长岩	154.00	1.03	0.162 363	0.355 315	Zhu *et al.*, 2011
英安岩	159.80	1.53	0.258 986	0.569 443	Zhu *et al.*, 2011
二长花岗岩	182.90	0.92	0.263 743	0.885 041	Zhu *et al.*, 2011
二长花岗岩	191.90	1.03	0.314 625	0.850 605	Zhu *et al.*, 2011
花岗闪长岩	193.20	0.45	0.327 711	1.069 529	Zhu *et al.*, 2011
二长花岗岩	193.60	1.08	0.406 652	0.556 256	Zhu *et al.*, 2011
正长花岗岩	194.90	0.89	0.725 794	0.475 859	Zhu *et al.*, 2011
花岗闪长岩	201.30	1.51	0.390 234	1.442 103	Zhu *et al.*, 2011

床主要分布于在侏罗纪时期高氧逸度、低含水量或低氧逸度及含水量岩浆区域(图 2、图 3),其中位于前者范围内的矿床规模相对较大(例如甲玛、驱龙超大型矿床)。

岩浆中较高的氧逸度会增加硫化物的溶解度,并抑制深部地壳岩浆储库的早期硫化物饱和,同时增加了斑岩 Cu 矿的成矿潜力。然而,当氧逸度作为控制硫化物饱和的单一变量时,在 1~1.5 GPa 的压力下,需要十分高的氧逸度(f_{O_2}>NNO+3)才能抑制硫化物饱和(Matjuschkin *et al.*, 2016)。这解释了分布有大量中新世斑岩 Cu 矿床的高氧逸度岩浆区域为何在侏罗纪未成矿。前人研究表明,除了氧逸度外,岩浆含水量也能控制硫化物的溶解度(Moretti and Baker, 2008; Fortin *et al.*, 2015; Xu *et al.*, 2022b)。在较低的地壳压力和中高的氧逸度条件下,水可以显著增加硫化物的溶解度(Matjuschkin *et al.*, 2016; Xu *et al.*, 2022b)。因此在岩浆含水量较高时,在更温和的氧逸度条件下就能抑制岛弧岩浆中硫化物的饱和(Wang *et al.*, 2024)。总之,较高的氧逸度和含水量相结合,通过抑制深部地壳岩浆储库的早期硫化物饱和,为斑岩矿床的形成提供了有利条件(Xu *et al.*, 2022b; Wang *et al.*, 2024)。在侏罗纪时期,高氧逸度和含水量岩浆区域内(图 3、图 4),通过抑制地壳深部的早期硫化物饱和,为 S 和 Cu、Au 等从深部地壳岩浆储库向浅部储库的迁移和聚集提供了有效机制,为侏罗纪斑岩 Cu 矿床的形成提供了充足的金属来源。在侏罗纪时期,高氧逸度、低含水量岩浆或低氧逸度及含水量岩浆区域内,氧逸度(最高 △FMQ =2.76)未达到可单独抑制硫化物饱和的条件,且二者相互作用也未达到此条件,因此在深部地壳发生早期硫化物饱和。由于硫化物/熔体的分配系数 DCu sulfur/melt>1 000 (Park *et al.*, 2021),硫化物的分离将有效地从熔体中分离 Cu,从而形成大量含 Cu 的下地壳堆晶,这解释了分布有大量中新世斑岩 Cu 矿床的高氧逸度、低含水量岩浆或低氧逸度及含水量岩浆区域为何在侏罗纪未成矿。Nd 同位素填图结果显示,侏罗纪斑岩 Cu 矿床主要发育在侏罗纪新生地壳,而中新世斑岩 Cu 矿床主要发育在侏罗纪时期新老地壳边界附近(图 2、图 3),可能暗示古老地壳的混入促进了侏罗纪岩浆早期硫化物饱和及含 Cu 下地壳堆晶的形成,抑制了其在侏罗纪成矿。新老地壳接触界面附近与高氧逸度、低含水量岩浆以及低氧逸度、含水量岩浆区域基本对应(图 2、图 3、图 4、图 5),表明古老地壳组分的混入可能降低了岩浆的氧逸度和或含水量。中新世与成矿相关的埃达克质岩具有与侏罗纪弧岩浆岩相似的 Sr-Nd、Hf 和 O 同位素组成(Zheng *et al.*, 2012; Hou *et al.*, 2015a; Wang *et al.*, 2017b),表明前者可能主要来源于侏罗纪新生镁铁质地壳的重熔(Hou *et al.*, 2015a)。印度-欧亚大陆碰撞后期(<25 Ma)俯冲的印度大陆板片撕裂(Hou *et al.*, 2015c; Hou *et al.*, 2023),导致热软流圈熔体底侵,触发了侏罗纪含 Cu 下地壳堆晶重熔,为中新世斑岩矿床的形成提供了丰富的硫和金属等成矿组分。

5　结论

(1) 侏罗纪与俯冲相关的斑岩 Cu-Au 矿床主要发育于侏罗纪新生地壳,而中新世与碰撞相关的斑岩 Cu-Mo 矿床产在侏罗纪时期新老地壳接触边界附近。

(2) 在侏罗纪时期,与俯冲相关的斑岩 Cu-Au 矿床处于高氧逸度、含水量岩浆区域,而中新世与碰撞相关的斑岩 Cu-Mo 矿床在高氧逸度、低含水量岩浆或低氧逸度、含水量岩浆区域均有发育。

(3) 新老地壳接触界面附近与高氧逸度、低含水量岩浆和低氧逸度、含水量岩浆区域基本对应,表明古老地区组分的混入可能降低了岩浆的氧逸度和或含水量,导致其未能有效抑制深部岩浆的早期硫化物饱和,诱发了含 Cu 下地壳堆晶的形成,为中新世碰撞相关斑岩的形成储蓄了充足的金属。

References

Ballard J R, Palin J M and Campbell I H. 2002. Relative oxidation states of magmas inferred from Ce(Ⅳ)/Ce(Ⅲ) in zircon: Application to porphyry copper deposits of northern Chile[J]. Contributions to Mineralogy and Petrology, 144(3): 347~364.

Bao X S, He W Y, Mao J W, *et al*. 2023. Redox states and genesis of Cu- and Au-mineralized granite porphyries in the Jinshajiang Cu-Au metallogenic belt, SW China: Studies on the zircon chemistry[J]. Mineralium Deposita, 58(6): 1 123~1 142.

Belousova E A, Kostitsyn Y A, Griffin W L, *et al*. 2010. The growth of the continental crust: Constraints from zircon Hf-isotope data[J]. Lithos, 119(3~4): 457~466.

Blisniuk P M, Hacker B R, Glodny J, *et al*. 2001. Normal faulting in

central Tibet since at least 13.5 Myr ago[J]. Nature, 412(6 847): 628~632.

Brounce M N, Kelley K A and Cottrell E. 2014. Variations in $Fe^{3+}/\sum Fe$ of Mariana arc basalts and mantle wedge f_{O_2}[J]. Journal of Petrology, 55(12): 2 513~2 536.

Champion D. 2013. Neodymium depleted mantle model age map of Australia: Explanatory notes and user guide[J]. Australia: Geoscience Australia.

Champion D C and Huston D L. 2016. Radiogenic isotopes, ore deposits and metallogenic terranes: Novel approaches based on regional isotopic maps and the mineral systems concept[J]. Ore Geology Reviews, 76: 229~256.

Chen X L, Liang H Y, Zhang J, *et al*. 2019a. Geochemical characteristics and magma fertility for the Jurassic arc rocks in the Gangdese belt, Tibet[J]. Ore Geology Reviews, 115: 103169.

Chen X L, Liang H Y, Zhang J, *et al*. 2020. Geochemical characteristics and oxidation states of the Xietongmen ore-bearing porphyries: Implication for the genetic types of the Xietongmen No. I and No. II deposits, southern Tibet[J]. Geological Journal, 55(6): 4 691~4 712.

Chen X L, Richards J P, Liang H Y, *et al*. 2019b. Contrasting arc magma fertilities in the gangdese belt, southern Tibet: Evidence from geochemical variations of Jurassic volcanic rocks[J]. Lithos, 324~325: 789~802.

Chu M F, Chung S L, Song B, *et al*. 2006. Zircon U-Pb and Hf isotope constraints on the Mesozoic tectonics and crustal evolution of southern Tibet[J]. Geology, 34(9): 745.

Chung S L, Liu D Y, Ji J Q, *et al*. 2003. Adakites from continental collision zones: Melting of thickened lower crust beneath southern Tibet [J]. Geology, 31(11): 1 021.

Coleman M and Hodges K. 1995. Evidence for Tibetan Plateau uplift before 14 Myr ago from a new minimum age for east-west extension[J]. Nature, 374(6517): 49~52.

DePaolo D J. 1988. Age dependence of the composition of continental crust: Evidence from Nd isotopic variations in granitic rocks [J]. Earth and Planetary Science Letters, 90(3): 263~271.

DePaolo D J, Linn A M and Schubert G. 1991. The continental crustal age distribution: Methods of determining mantle separation ages from Sm-Nd isotopic data and application to the southwestern United States [J]. Journal of Geophysical Research: Solid Earth, 96(B2): 2 071~2 088.

Davidson J P. 1996. Deciphering mantle and crustal signatures in subduction zone magmatism[J]. Geophysical Monograph Series, 96: 251~262.

Dong Guochen, Mo Xuanxue, Zhao Zhidan, *et al*. 2006. Magma mixing in middle part of gangdise magma belt: Evidences from granitoid complex[J]. Acta Petrologica Sinica, 22(4): 835~844 (in Chinese with English abstract).

Dong Xin and Zhang Zeming. 2013. Genesis and tectonic significance of the Early Jurassic magmatic rocks from the southern Lhasa terrane[J]. Acta Petrologica Sinica, 29(6): 1 933~1 948 (in Chinese with English abstract).

de Hoog J C M, Mason P R D and van Bergen M J. 2001. Sulfur and chalcophile elements in subduction zones: Constraints from a laser ablation ICP-MS study of melt inclusions from galunggung volcano, Indonesia[J]. Geochimica et Cosmochimica Acta, 65(18): 3 147~3 164.

Fortin M A, Riddle J, Desjardins-Langlais Y, *et al*. 2015. The effect of water on the sulfur concentration at sulfide saturation (SCSS) in natural melts[J]. Geochimica et Cosmochimica Acta, 160: 100~116.

Guo L, Zhang H F, Harris N, *et al*. 2011. Origin and evolution of multistage felsic melts in eastern gangdese belt: Constraints from U-Pb zircon dating and Hf isotopic composition[J]. Lithos, 127(1~2): 54~67.

Granseth A, Slagstad T, Roberts N M W, *et al*. 2021. Multi-isotope tracing of the 1.3-0.9 Ga evolution of Fennoscandia: crustal growth during the Sveconorwegian orogeny[J]. Gondwana Research, 91: 31~39.

Groulier P A, Turlin F, André-Mayer A S, *et al*. 2020. Silicate-carbonate liquid immiscibility: Insights from the crevier alkaline intrusion (Quebec)[J]. Journal of Petrology, 61(3): egaa033.

Hawkesworth C J, Dhuime B, Pietranik A B, *et al*. 2010. The generation and evolution of the continental crust[J]. Journal of the Geological Society, 167(2): 229~248.

Hou Z Q and Cook N J. 2009. Metallogenesis of the Tibetan collisional orogen: A review and introduction to the special issue[J]. Ore Geology Reviews, 36(1~3): 2~24.

Hou Z Q, Duan L F, Lu Y J, *et al*. 2015a. Lithospheric architecture of the Lhasa terrane and its control on ore deposits in the Himalayan-Tibetan Orogen[J]. Economic Geology, 110(6): 1 541~1 575.

Hou Z Q, Gao Y F, Qu X M, *et al*. 2004. Origin of adakitic intrusives generated during mid-Miocene east-west extension in southern Tibet [J]. Earth and Planetary Science Letters, 220(1~2): 139~155.

Hou Z Q, Li Q Y, Gao Y F, *et al*. 2015b. Lower-Crustal Magmatic Hornblendite in North China Craton: Insight into the Genesis of Porphyry Cu Deposits[J]. Economic Geology, 110 (7): 1 879~1 904.

Hou Zengqian and Wang Tao. 2018. Isotopic mapping and deep material probing (Ⅱ): Imaging crustal architecture and its control on mineral systems[J]. Earth Science Frontiers, 25(6): 20~41 (in Chinese with English abstract).

Hou Z Q, Wang R, Zhang H J, *et al*. 2023. Formation of giant copper deposits in Tibet driven by tearing of the subducted Indian plate[J]. Earth-Science Reviews, 243: 104482.

Hou Z, Yang Z, Lu Y, *et al*. 2015c. A genetic linkage between subduction- and collision-related porphyry Cu deposits in continental collision zones[J]. Geology, 43(3): 247~250.

Hou Z Q, Yang Z M, Qu X M, *et al*. 2009. The Miocene Gangdese porphyry copper belt generated during post-collisional extension in the Tibetan Orogen[J]. Ore Geology Reviews, 36(1~3): 25~51.

Hou Z Q and Zhang H R. 2015. Geodynamics and metallogeny of the eastern Tethyan metallogenic domain[J]. Ore Geology Reviews, 70: 346~384.

Hou Zengqian, Zheng Yuanchuan, Lu Zhanwu, *et al*. 2020. The thick crust of Qinghai-Tibet Plateau: Growth, thickening and evolution[J]. Acta Geologica Sinica, 94(10): 2 797~2 815 (in Chinese).

Jacobsen S B and Wasserburg G J. 1980. Sm-Nd isotopic evolution of chondrites[J]. Earth and Planetary Science Letters, 50(1): 139~155.

Ji W Q, Wu F Y, Chung S L, *et al*. 2009. Zircon U-Pb geochronology and Hf isotopic constraints on petrogenesis of the Gangdese batholith, southern Tibet[J]. Chemical Geology, 262(3~4): 229~245.

Kang Z Q, Xu J F, Wilde S A, *et al*. 2014. Geochronology and geochemistry of the Sangri Group volcanic rocks, southern Lhasa terrane: Implications for the early subduction history of the neo-Tethys and gangdese magmatic arc[J]. Lithos, 200: 157~168.

Kelley K A and Cottrell E. 2009. Water and the oxidation state of subduction zone magmas[J]. Science, 325(5940): 605~607.

Kovalenko V I, Yarmolyuk V V, Kovach V P, *et al*. 2004. Isotope provinces, mechanisms of generation and sources of the continental crust in the central Asian mobile belt: Geological and isotopic evidence[J]. Journal of Asian Earth Sciences, 23(5): 605~627.

Lang Xinghai, Chen Yuchuan, Tang Juxing, *et al*. 2010. Characteristics of rock geochemistry of orebody No. I in the Xiongcun porphyry copper-gold metallogenic district, Xietongmen County, Tibet: Constraints on metallogenic tectonic settings[J]. Geology and Exploration, 46(5): 887~898 (in Chinese with English abstract).

Lang Xinghai, Guo Wenbo, Wang Xuhui, *et al*. 2019. Petrogenesis and tectonic implications of the ore-bearing porphyries in the Xiongcun district: Constraints from the geochronology and geochemistry[J]. Acta Petrologica Sinica, 35(7): 2 105~2 123 (in Chinese with English abstract).

Lang X H, Tang J X, Li Z J, *et al*. 2014. U-Pb and Re-Os geochronological evidence for the Jurassic porphyry metallogenic event of the Xiongcun district in the Gangdese porphyry copper belt, southern Tibet, PRC[J]. Journal of Asian Earth Sciences, 79: 608~622.

Lang X H, Wang X H, Deng Y L, *et al*. 2019. Early Jurassic volcanic rocks in the Xiongcun district, southern Lhasa subterrane, Tibet: Implications for the tectono-magmatic events associated with the early evolution of the neo-Tethys ocean[J]. Lithos, 340: 166~180.

Lang X H, Wang X H, Tang J X, *et al*. 2018. Composition and age of Jurassic diabase dikes in the Xiongcun porphyry copper-gold district, southern margin of the Lhasa terrane, Tibet, China: Petrogenesis and tectonic setting[J]. Geological Journal, 53(5): 1 973~1 993.

Li Chengzhi, Yang Wenguang, Zhu Lidong, *et al*. 2019. Zircon u-Pb age, geochemical characteristics and diagenetic dynamic background of the cuobulaguo granites in the southern margin of Lhasa terrane[J]. Mineralogy and Petrology, 39(2): 45~57 (in Chinese with English abstract).

Li L, Xie H, Lang X H, *et al*. 2022. Petrogenesis of Early-Middle Jurassic gabbros in southern Tibet with implications for crustal growth in the southern Lhasa subterrane[J]. International Geology Review, 64(12): 1 755~1 780.

Liu Qisheng, Jiang Wan, Jian Ping, *et al*. 2006. Zircon SHRIMP U-Pb age and petrochemical and geochemical features of Mesozoic muscovite monzonitic granite at Ningzhong, Tibet[J]. Acta Petrologica Sinica, 22(3): 643~652 (in Chinese with English abstract).

Loader M A, Wilkinson J J and Armstrong R N. 2017. The effect of titanite crystallisation on Eu and Ce anomalies in zircon and its implications for the assessment of porphyry Cu deposit fertility[J]. Earth and Planetary Science Letters, 472: 107~119.

Loucks R R, Fiorentini M L and Henríquez G J. 2020. New magmatic oxybarometer using trace elements in zircon[J]. Journal of Petrology, 61(3): egaa034.

Lu Yongjun, Smithies R H, Wingate M T D, *et al*. 2019. Zircon fingerprinting of magmatic-hydrothermal systems in the Archean Yilgarn Craton[J]. Geological Survey of Western Australia, 197: 22.

Ma S W, Meng Y K, Xu Z Q, *et al*. 2017a. The discovery of Late Triassic mylonitic granite and geologic significance in the middle Gangdese batholiths, southern Tibet[J]. Journal of Geodynamics, 104: 49~64.

Ma X X, Xu Z Q, Chen X J, *et al*. 2017b. The origin and tectonic significance of the volcanic rocks of the Yeba Formation in the Gangdese magmatic belt, South Tibet[J]. Journal of Earth Science, 28(2): 265~282.

Matjuschkin V, Blundy J D and Brooker R A. 2016. The effect of pressure on sulphur speciation in mid- to deep-crustal arc magmas and implications for the formation of porphyry copper deposits[J]. Contributions to Mineralogy and Petrology, 171(7): 66.

Mole D R, Fiorentini M L, Cassidy K F, *et al*. 2015. Crustal evolution, intra-cratonic architecture and the metallogeny of an Archaean craton

[J]. Geological Society, London, Special Publications, 393(1): 23~80.

Mole D R, Fiorentini M L, Thebaud N, *et al*. 2014. Archean komatiite volcanism controlled by the evolution of early continents[J]. Proceedings of the National Academy of Sciences of the United States of America, 111(28): 10 083~10 088.

Moore G and Carmichael I S E. 1998. The hydrous phase equilibria (to 3 kbar) of an andesite and basaltic andesite from western Mexico: Constraints on water content and conditions of phenocryst growth[J]. Contributions to Mineralogy and Petrology, 130(3): 304~319.

Moretti R and Baker D R. 2008. Modeling the interplay of f_{O_2} and f_{S_2} along the FeS-silicate melt equilibrium[J]. Chemical Geology, 256(3~4): 286~298.

Müntener O, Kelemen P B and Grove T L. 2001. The role of H_2O during crystallization of primitive arc magmas under uppermost mantle conditions and genesis of igneous pyroxenites: An experimental study[J]. Contributions to Mineralogy and Petrology, 141(6): 643~658.

Nathwani C L, Simmons A T, Large S J E, *et al*. 2021. From long-lived batholith construction to giant porphyry copper deposit formation: Petrological and zircon chemical evolution of the quellaveco district, southern Peru[J]. Contributions to Mineralogy and Petrology, 176(2): 12.

Pan G T, Wang L Q, Li R S, *et al*. 2012. Tectonic evolution of the Qinghai-Tibet Plateau[J]. Journal of Asian Earth Sciences, 53: 3~14.

Park J W, Campbell I H, Chiaradia M, *et al*. 2021. Crustal magmatic controls on the formation of porphyry copper deposits[J]. Nature Reviews Earth & Environment, 2: 542~557.

Qu Xiaoming, Hou Zengqian, Mo Xuanxue, *et al*. 2006. Relationship between gangdese porphyry copper deposits and uplifting of southern Tibet Plateau: Evidence from multistage zircon of ore-bearing porphyries[J]. Mineral Deposits, 25(4): 388~400 (in Chinese with English abstract).

Rezeau H, Moritz R, Wotzlaw J F, *et al*. 2019. Zircon petrochronology of the Meghri-Ordubad pluton, Lesser Caucasus: Fingerprinting igneous processes and implications for the exploration of porphyry Cu-Mo deposits[J]. Economic Geology, 114(7): 1 365~1 388.

Richards J P. 2003. Tectono-magmatic precursors for porphyry Cu-(Mo-Au) deposit formation[J]. Economic Geology, 98(8): 1 515~1 533.

Richards J P. 2009. Postsubduction porphyry Cu-Au and epithermal Au deposits: Products of remelting of subduction-modified lithosphere[J]. Geology, 37(3): 247~250.

Richards J P. 2011. Magmatic to hydrothermal metal fluxes in convergent and collided margins[J]. Ore Geology Reviews, 40(1): 1~26.

Richards J P. 2015. Tectonic, magmatic, and metallogenic evolution of the Tethyan Orogen: From subduction to collision[J]. Ore Geology Reviews, 70: 323~345.

Ridolfi F, Renzulli A and Puerini M. 2010. Stability and chemical equilibrium of amphibole in calc-alkaline magmas: An overview, new thermobarometric formulations and application to subduction-related volcanoes[J]. Contributions to Mineralogy and Petrology, 160(1): 45~66.

Sillitoe R H. 2010. Porphyry copper systems[J]. Economic Geology, 105(1): 3~41.

Tafti R, Mortensen J K, Lang J R, *et al*. 2009. Jurassic u-Pb and re-Os ages for the newly discovered Xietongmen Cu-Au porphyry district, Tibet, prc: Implications for metallogenic epochs in the southern gangdese belt[J]. Economic Geology, 104(1): 127~136.

Trail D, Watson E B and Tailby N D. 2011. The oxidation state of Hadean magmas and implications for early Earth's atmosphere[J]. Nature, 480(7375): 79~82.

Turlin F, Vanderhaeghe O, Gervais F, *et al*. 2019. Petrogenesis of LREE-rich pegmatitic granite dykes in the central Grenville Province by partial melting of Paleoproterozoic-Archean metasedimentary rocks: Evidence from zircon U-Pb-Hf-O isotope and trace element analyses[J]. Precambrian Research, 327: 327~360.

Wang C M, Bagas L, Lu Y J, *et al*. 2016. Terrane boundary and spatio-temporal distribution of ore deposits in the Sanjiang Tethyan Orogen: Insights from zircon Hf-isotopic mapping[J]. Earth-Science Reviews, 156: 39~65.

Wang Li. 2013. Late Jurassic Early Eocene Magmatic Activity on the Southeastern Edge of the Gangdise Rock Foundation in the southern Qinghai Tibet Plateau[D]. Beijing: Chinese Academy of Geological Sciences (in Chinese with English abstract).

Wang R Q, Qiu J S, Yu S B, *et al*. 2017a. Crust-mantle interaction during Early Jurassic subduction of neo-Tethyan oceanic slab: Evidence from the dongga gabbro-granite complex in the southern Lhasa subterrane, Tibet[J]. Lithos, 292: 262~277.

Wang R, Tafti R, Hou Z Q, *et al*. 2017b. Across-arc geochemical variation in the Jurassic magmatic zone, southern Tibet: Implication for continental arc-related porphyry Cu-Au mineralization[J]. Chemical Geology, 451: 116~134.

Wang T, Jahn B, Kovach V P, *et al*. 2009. Nd-Sr isotopic mapping of the Chinese Altai and implications for continental growth in the Central Asian Orogenic Belt[J]. Lithos, 110 (1): 359~372.

Wang Xuhui. 2019. Geochronology and Geochemical Characteristics of Jurassic Rocks in Ruocuo County, Tibet[D]. Chengdu: Chengdu University of Technology (in Chinese with English abstract).

Wang X, Lang X, Tang J, *et al*. 2019. Early-Middle Jurassic (182~

170 Ma) Ruocuo adakitic porphyries, southern margin of the Lhasa terrane, Tibet: Implications for geodynamic setting and porphyry Cu-Au mineralization[J]. Journal of Asian Earth Sciences, 173: 336~351.

Wang X H, Lang X H, Turlin F, *et al*. 2024. Copper behavior in arc-back-arc systems: Insights into the porphyry Cu metallogeny of the gangdese belt, southern Tibet[J]. Mineralium Deposita, 59(1): 133~154.

Wu C, Chen H Y and Lu Y J. 2021. Magmatic water content and crustal evolution control on porphyry systems: Insights from the Central Asian Orogenic Belt[J]. Journal of Petrology, 62(2): egab021.

Wu F Y, Sun D Y, Li H M, *et al*. 2002. A-type granites in Northeastern China: Age and geochemical constraints on their petrogenesis[J]. Chemical Geology, 187(1~2): 143~173.

Xie F W, Tang J X, Chen Y C, *et al*. 2018a. Apatite and zircon geochemistry of Jurassic porphyries in the Xiongcun district, southern gangdese porphyry copper belt: Implications for petrogenesis and mineralization[J]. Ore Geology Reviews, 96: 98~114.

Xie F W, Tang J X, Jia M, *et al*. 2023. Zircon and apatite fingerprints on the magma fertility for the Jurassic igneous rocks in the southern Lhasa subterrane, Tibet[J]. Ore Geology Reviews, 161: 105662.

Xie F W, Tang J X, Lang X H, *et al*. 2018b. The different sources and petrogenesis of Jurassic intrusive rocks in the southern Lhasa subterrane, Tibet: Evidence from the trace element compositions of zircon, apatite, and titanite[J]. Lithos, 314: 447~462.

Xu B, Hou Z Q, Griffin W L, *et al*. 2021. Cenozoic lithospheric architecture and metallogenesis in Southeastern Tibet[J]. Earth-Science Reviews, 214: 103472.

Xu B, Hou Z Q, Griffin W L, *et al*. 2022a. Apatite halogens and Sr-O and zircon Hf-O isotopes: Recycled volatiles in Jurassic porphyry ore systems in southern Tibet[J]. Chemical Geology, 605: 120924.

Xu B, Hou Z Q, Zheng Y C, *et al*. 2017. In situ elemental and isotopic study of diorite intrusions: Implication for Jurassic arc magmatism and porphyry Cu-Au mineralisation in southern Tibet[J]. Ore Geology Reviews, 90: 1 063~1 077.

Xu L L, Zhu J J, Huang M L, *et al*. 2023. Genesis of hydrous-oxidized parental magmas for porphyry Cu (Mo, Au) deposits in a postcollisional setting: Examples from the Sanjiang Region, SW China[J]. Mineralium Deposita, 58(1): 161~196.

Xu P Y, Zheng Y C, Yang Z S, *et al*. 2020. Metallogeny of the continental collision-related Jiagang W-Mo deposit, Tibet: Evidence from geochronology and petrogenesis[J]. Ore Geology Reviews, 122: 103519.

Xu T, Liu X C, Xiong X L, *et al*. 2022b. Sulfur dissolution capacity of highly hydrated and fluid-saturated dacitic magmas at the lower crust and implications for porphyry deposit formation[J]. Geochimica et Cosmochimica Acta, 333: 107~123.

Xu W, Zhu D C, Wang Q, *et al*. 2019. Constructing the early Mesozoic gangdese crust in southern Tibet by hornblende-dominated magmatic differentiation[J]. Journal of Petrology, 60(3): 515~552.

Yang Z M, Goldfarb R and Chang Z S. 2016. Generation of postcol lisional porphyry copper deposits in southern Tibet triggered by subduction of the Indian continental plate[J]. SEG Special Publication, 19: 279~300.

Yang Zhiming, Hou Zengqian, Jiang Yingfei, *et al*. 2011. Sr-Nd-Pb and zircon Hf isotopic constraints on petrogenesis of the Late Jurassic granitic porphyry at Qulong, Tibet[J]. Acta Petrologica Sinica, 27(7): 2 003~2 010 (in Chinese with English abstract).

Yin A and Harrison T M. 2000. Geologic evolution of the Himalayan-Tibetan Orogen[J]. Annual Review of Earth and Planetary Sciences, 28: 211~280.

Yin Q, Lang X H, Cui Z W, *et al*. 2017. Geology and geochemistry constraints on the genesis of the Xiongcun No. 2 deposit porphyry Cu-Au deposit in the Xiongcun district, Gangdese porphyry copper belt, Tibet, China[J]. Appl. Ecol. Environ. Res., 15(3): 477~508.

Yu J X, Xu B, Zhao Y, *et al*. 2022. In situ Sr-O isotopic and elemental compositions of apatite and zircon from Pengcuolin granodiorites: Implications for Jurassic metallogenic variation in the southern Tibet[J]. Ore Geology Reviews, 145: 104869.

Yuan L L, Chai P, Hou Z Q, *et al*. 2023. Implications of Nd isotopic mapping for crustal composition and metallogenesis in the Sanjiang orogenic belt (SW China)[J]. Frontiers in Earth Science, 11: 1131338.

Zhang C, Liu L F, Santosh M, *et al*. 2017. Sediment recycling and crustal growth in the Central Asian Orogenic Belt: Evidence from Sr-Nd-Hf isotopes and trace elements in granitoids of the Chinese Altay[J]. Gondwana Research, 47: 142~160.

Zhang Hongfei, Xu Wangchun, Guo Jianqiu, *et al*. 2007. Zircon U-Pb and Hf isotopic composition of deformed granite in the southern margin of the gangdise belt, Tibet: Evidence for Early Jurassic subduction of neo-Tethyan oceanic slab[J]. Acta Petrologica Sinica, 23(6): 1 347~1 353 (in Chinese with English abstract).

Zhang K L, Shi Z M, Liao R, *et al*. 2020a. Petrogenesis and geological implications of the Oligocene mingze monzodiorites, southern Lhasa[J]. Minerals, 10(4): 301.

Zhang Y X, Gazel E, Gaetani G A, *et al*. 2021. Serpentinite-derived slab fluids control the oxidation state of the subarc mantle[J]. Science Advances, 7(48): eabj2515.

Zhang Z M, Ding H X, Palin R M, *et al*. 2020b. The lower crust of the Gangdese magmatic arc, southern Tibet, implication for the growth of

continental crust[J]. Gondwana Research, 77: 136~146.

Zhang Zeming, Dong Xin, Santosh M, *et al*. 2014. Metamorphism and tectonic evolution of the Lhasa terrane, Central Tibet[J]. Gondwana Research, 25(1): 170~189.

Zheng W B, Tang J X, Zhong K H, *et al*. 2016. Geology of the Jiama porphyry copper-polymetallic system, Lhasa Region, China[J]. Ore Geology Reviews, 74: 151~169.

Zheng Y C, Hou Z Q, Li Q Y, *et al*. 2012. Origin of late Oligocene adakitic intrusives in the southeastern Lhasa terrane: Evidence from in situ zircon U-Pb dating, Hf-O isotopes, and whole-rock geochemistry [J]. Lithos, 148: 296~311.

Zheng Y C, Shen Y, Wang L, *et al*. 2021. Collision-related porphyry Cu deposits formed by input of ultrapotassic melts into the sulfide-rich lower crust[J]. Terra Nova, 33(6): 582~589.

Zheng Y C, Wu C D, Tian S H, *et al*. 2020. Magmatic and structural controls on the tonnage and metal associations of collision-related porphyry copper deposits in southern Tibet[J]. Ore Geology Reviews, 122: 103509.

Zheng Y Y, Zhang G Y, Xu R K, *et al*. 2007. Geochronologic constraints on magmatic intrusions and mineralization of the Zhunuo porphyry copper deposit in Gangdese, Tibet[J]. Chinese Science Bulletin, 52(22): 3 139~3 147.

Zhu D C, Pan G T, Chung S L, *et al*. 2008. SHRIMP zircon age and geochemical constraints on the origin of lower Jurassic volcanic rocks from the yeba formation, southern gangdese, South Tibet[J]. International Geology Review, 50(5): 442~471.

Zhu Dicheng, Pan Guitang, Wang Liquan, *et al*. 2008. Tempo-spatial variations of Mesozoic magmatic rocks in the Gangdise belt, Tibet, China, with a discussion of geodynamic setting-related issues[J]. Geological Bulletin of China, 27(9): 1 535~1 550 (in Chinese with English abstract).

Zhu D C, Wang Q, Chung S L, *et al*. 2019. Gangdese magmatism in southern Tibet and India-Asia convergence since 120 Ma[J]. Geological Society, London, Special Publications, 483(1): 583~604.

Zhu D C, Zhao Z D, Niu Y L, *et al*. 2011. The Lhasa Terrane: Record of a microcontinent and its histories of drift and growth[J]. Earth and Planetary Science Letters, 301(1~2): 241~255.

Zhu D C, Zhao Z D, Niu Y L, *et al*. 2013. The origin and pre-Cenozoic evolution of the Tibetan Plateau[J]. Gondwana Research, 23(4): 1 429~1 454.

Zou Yinqiao, Huang Wenting, Liang Huaying, *et al*. 2015. Identification of porphyry genetically associated with mineralization and its zircon U-Pb and biotite Ar-Ar age of the Xiongcun Cu-Au deposit, southern Gangdese, Tibet[J]. Acta Petrologica Sinica, 31(7): 2 053~2 062 (in Chinese with English abstract).

附中文参考文献

董国臣, 莫宣学, 赵志丹, 等. 2006. 冈底斯岩浆带中段岩浆混合作用: 来自花岗杂岩的证据[J]. 岩石学报, 22(4): 835~844.

董 昕, 张泽明. 2013. 拉萨地体南部早侏罗世岩浆岩的成因和构造意义[J]. 岩石学报, 29(6): 1 933~1 948.

侯增谦, 王 涛. 2018. 同位素填图与深部物质探测(Ⅱ): 揭示地壳三维架构与区域成矿规律[J]. 地学前缘, 25(6): 20~41.

侯增谦, 郑远川, 卢占武, 等. 2020. 青藏高原巨厚地壳: 生长、加厚与演化[J]. 地质学报, 94(10): 2 797~2 815.

郎兴海, 陈毓川, 唐菊兴, 等. 2010. 西藏谢通门县雄村斑岩型铜金矿集区Ⅰ号矿体的岩石地球化学特征:对成矿构造背景的约束[J]. 地质与勘探, 46(5): 887~898.

郎兴海, 郭文铂, 王旭辉, 等. 2019. 西藏雄村矿集区含矿斑岩成因及构造意义——来自年代学及地球化学的约束[J]. 岩石学报, 35(7): 2 105~2 123.

李成志, 杨文光, 朱利东, 等. 2019. 拉萨地体南缘错布拉果花岗岩体锆石 U-Pb 年龄、地球化学特征及成岩动力学背景[J]. 矿物岩石, 39(2): 45~57.

刘琦胜, 江 万, 简 平, 等. 2006. 宁中白云母二长花岗岩 SHRIMP 锆石 U-Pb 年龄及岩石地球化学特征[J]. 岩石学报, 22(3): 643~652.

曲晓明, 侯增谦, 莫宣学, 等. 2006. 冈底斯斑岩铜矿与南部青藏高原隆升之关系——来自含矿斑岩中多阶段锆石的证据[J]. 矿床地质, 25(4): 388~400.

王 莉. 2017. 青藏高原南部冈底斯岩基东南缘晚侏罗世—早始新世岩浆作用[D]. 北京: 中国地质科学院.

王旭辉. 2019. 西藏拉孜县若措侏罗纪岩体年代学及地球化学特征研究[D]. 成都: 成都理工大学.

杨志明, 侯增谦, 江迎飞, 等. 2011. 西藏驱龙矿区早侏罗世斑岩的 Sr-Nd-Pb 及锆石 Hf 同位素研究[J]. 岩石学报, 27(7): 2 003~2 010.

张宏飞, 徐旺春, 郭建秋, 等. 2007. 冈底斯南缘变形花岗岩锆石 U-Pb 年龄和 Hf 同位素组成: 新特提斯洋早侏罗世俯冲作用的证据[J]. 岩石学报, 23(6): 1 347~1 353.

郑有业, 张刚阳, 许荣科, 等. 2007. 西藏冈底斯朱诺斑岩铜矿床成岩成矿时代约束[J]. 科学通报, 52(21): 2 542~2 548.

朱弟成, 潘桂棠, 王立全, 等. 2008. 西藏冈底斯带中生代岩浆岩的时空分布和相关问题的讨论[J]. 地质通报, 27(9): 1 535~1 550.

邹银桥, 黄文婷, 梁华英, 等. 2015. 西藏冈底斯南缘雄村铜金矿床成矿斑岩厘定及其锆石 U-Pb 和黑云母 Ar-Ar 年龄分析[J]. 岩石学报, 31(7): 2 053~2 062.